Materials Science & Engineering C 123 (2021) 112023

Contents lists available at ScienceDirect

Materials Science & Engineering C

journal homepage: www.elsevier.com/locate/msec

One-minute and green synthesis of magnetic iron oxide nanoparticles assisted by design of experiments and high energy ultrasound: Application to biosensing and immunoprecipitation

Christian Hazael Pérez-Beltrán [a,b], Juan José García-Guzmán [a], Bibiana Ferreira [c,d,e], Osvaldo Estévez-Hernández [f], David López-Iglesias [a], Laura Cubillana-Aguilera [a], Wolfgang Link [g], N. Stănică [h], Ana Maria Rosa da Costa [b,i,*], José María Palacios-Santander [a,**]

[a] Institute of Research on Electron Microscopy and Materials (IMEYMAT), Department of Analytical Chemistry, Faculty of Sciences, Campus de Excelencia Internacional del Mar (CEIMAR), University of Cádiz, Campus Universitario de Puerto Real, Polígono del Río San Pedro, S/N, 11510 Puerto Real, Cádiz, Spain
[b] Faculty of Science and Technology, Universidade do Algarve, Campus Gambelas, Faro 8005-139, Portugal
[c] Centre for Biomedical Research (CBMR), Universidade do Algarve, Campus Gambelas, Faro 8005-139, Portugal
[d] Algarve Biomedical Center (ABC), University of Algarve, Campus de Gambelas, 8005-139 Faro, Portugal
[e] Regenerative Medicine Program, Department of Biomedical Sciences and Medicine, University of Algarve, Campus de Gambelas, 8005-139 Faro, Portugal
[f] Instituto de Ciencia y Tecnología de Materiales (IMRE), Universidad de La Habana, Zapata y G, Vedado 10400, La Habana, Cuba
[g] Instituto de Investigaciones Biomédicas "Alberto Sols" (CSIC-UAM), Arturo Duperier 4, 28029 Madrid, Spain
[h] Institute of Physical Chemistry 'Ilie Murgulescu' of the Romanian Academy, 202 Splaiul Independentei, 060021 Bucharest, Romania
[i] Algarve Chemistry Research Centre (CIQA), Universidade do Algarve, Campus Gambelas, Faro 8005-139, Portugal

ARTICLE INFO

Keywords:
Magnetic nanoparticles
1 min-synthesis
Design of experiments
High-energy ultrasound
Iron oxides
Biosensing
Immunoprecipitation

ABSTRACT

The present study is focused on the ultrafast and green synthesis, via the co-precipitation method, of magnetic nanoparticles (MNPs) based on iron oxides using design of experiments (DOE) and high energy sonochemical approach, considering two main factors: amplitude (energy) of the ultrasound probe and sonication time. The combination of these techniques allowed the development of a novel one-minute green synthesis, which drastically reduced the amount of consumed energy, solvents, reagents, time and produced residues. This green sonochemical synthesis permitted to obtain mean particle sizes of 11 ± 2 nm under the optimized conditions of amplitude = 40% (2826 J) and time = 1 min. Their composition, structure, size, morphology and magnetic properties were assessed through X-ray diffraction (XRD), Fourier transform infrared spectroscopy (FTIR), thermogravimetric analysis (TGA), scanning and transmission electron microscopy (SEM & TEM), and vibrating sample magnetometry (VSM). The characterization results indicate the proper formation of MNPs, and the correct functionalization of MNPs with different coating agents. The functionalized MNPs were used as: i) biosensor, which could detect mercury in water in the range of 0.030–0.060 ppm, and ii) support onto which polyclonal antibodies were anchored and successfully bound to an osteosarcoma cell line expressing the target protein (TRIB2-GFP), as part of an immunoprecipitation assay.

1. Introduction

Magnetic nanoparticles (MNPs) based on iron oxides, especially magnetite, have been studied since 1981 [1]. Their importance and potential applications due to their special properties, such as superparamagnetism, high field irreversibility, high saturation field, biocompatibility, long durability, low toxicity and low cost [2,3] are well known. These features depend on their size, shape, magnetization and monodispersive character [2,4].

The aforementioned attributes have promoted the use of MNPs and their nanohybrids for different applications, such as magnetic resonance imaging [5], for monitoring inhibitory drugs [6], in biomedicine for diagnosing diseases, drug delivery [7] and hyperthermia [8], and as electrocatalyst for methanol electro-oxidation [9], among others.

* Correspondence to: A. Rosa da Costa, Faculty of Science and Technology, Universidade do Algarve, Campus Gambelas, Faro 8005-139, Portugal.
** Corresponding author.
E-mail addresses: amcosta@ualg.pt (A.M. Rosa da Costa), josem.palacios@uca.es (J.M. Palacios-Santander).

https://doi.org/10.1016/j.msec.2021.112023
Received 20 November 2020; Received in revised form 8 February 2021; Accepted 2 March 2021
Available online 10 March 2021

The usual techniques employed for the synthesis of MNPs include chemical vapor deposition [10], the polyol process [11], and iron salts co-precipitation [12,13]. The latter is the most common route for MNPs production due to its simplicity, low cost and high yields. However, some drawbacks are the: 1) particle size control, 2) broad size distribution, 3) time consuming, and 4) various resultant phases [14], which could be ferrihydrite, akagenite (FeOOH), goethite (α-FeOOH), hematite (α-Fe_2O_3), maghemite ($^{\gamma}$-Fe_2O_3), and magnetite (Fe_3O_4) [15,16]. In order to overcome these problems, the influence of various parameters (temperature, pH, precursors and use of surfactants) over the particle size, size distribution and resultant phases has been evaluated [2,4,17].

For the last decade, the concept of Green Chemistry has become a transversal topic in all fields of Analytical Chemistry and has helped to create conscious about taking care of the environment through the development of green methods that fulfill the 12 Green Analytical principles [18]. Nowadays, sonochemistry has attracted much attention, particularly the sonochemical synthesis, which is considered a green and ecological technique [19], as it minimizes the consumption of energy and non-green solvents, produces a smaller amount of residues, and drastically decreases reaction time, thus being considered a low cost technique [18,21,22]. Its effectiveness is the result of the acoustic cavitation phenomenon that consists on the formation, growth and collapse of bubbles in liquid medium, generating free radicals caused by the extreme conditions (≈5000 K, ≈500 bar, cooling rate 10^{10} K·s^{-1}) at the moment of the implosive collapse of the bubbles [20].

Given the importance of sonochemical synthesis in Green Chemistry, several studies have been successfully reported [23–28].

In particular, the sonochemical synthesis of MNPs has already been addressed [29,30]. On the one hand, high temperature values (90, 95 and 100 °C) were employed during 30 min at 1200 W, obtaining MNPs between 3 and 11 nm with values of saturation magnetization (Ms) around 35 emu/g [29]. On the other hand, the sonochemical synthesis of MNPs in the presence of three different concentrations of chitosan and no temperature control led to mean particle sizes between 10 and 25 nm and Ms. values from 36 to 57 emu/g using an amplitude of 50% for 2 min [30]. Nonetheless, the variable of amplitude (energy) was not controlled, generating high energy consumption. Additionally, the effect of interaction among amplitude (energy) and time over the particle size was not addressed.

DOE, specifically response surface methodology (RSM), has been used for different applications, such as liquid-phase microextraction [31], assessment of the performance of an engine using alternative fuel [32], and the syntheses of nanoparticles [26], within others. The main advantage of DOE is the possibility of performing a minimum number of experiments in order to understand the interacting factors of the system for optimization and prediction purposes [33,34].

The usefulness of bare MNPs can be enhanced through functionalization with organic molecules or polymers for particular applications, such as biosensing and immunoprecipitation. These reactive sites, especially carboxylic groups, are linked to the bare MNPs and further used to anchor specific biomolecules to detect the target analyte as it is demonstrated within this research.

The current study applies DOE to study the influence of two important factors in the sonochemical synthesis of MNPs, amplitude (energy) and time, as well as their interactions and effect on the particle size of the resulting MNPs. Statistical analysis of experimental results is also performed, considering a minimum number of syntheses, thus leading to the optimization of the process in terms of the established factors in the DOE. Additionally, minimization of the MNPs size, a narrow size distribution and higher saturation magnetization values are pursued.

Hence, in this paper, MNPs were synthesized in one minute via the co-precipitation method of Fe^{2+} and Fe^{3+} in basic media assisted by DOE and through the application of high energy ultrasound. Furthermore, the MNPs were successfully coated with organic species including typical biomolecules and drugs linkers, such as polydopamine (PDA), citric acid (ACS), isonipecotic acid (ISNPA), mercaptopropionic acid (MPA), sodium citrate (SC) and chitosan (CS). The composition, structure, size and morphology of the coated MNPs were studied through X-ray diffraction (XRD), Fourier transform infrared spectroscopy (FTIR), thermogravimetric analysis (TGA) and scanning and transmission electron microscopy (SEM and TEM). The magnetic properties of the samples were investigated through vibrating sample magnetometry (VSM). The PDA-coated MNPs with the horseradish peroxidase (HRP) enzyme were used to detect the maximum contaminant level of mercury (Hg^{2+}) in water (2 ppb or 2 μg/L = 10 nM, US Environmental Protection Agency-USEPA) using a direct inhibition strategy based on enzyme-linked colorimetric assays. Moreover, the coated MNPs were used to attach polyclonal antibodies on their surfaces, and employed as a tool for an immunoprecipitation study. Both applications were successfully developed, demonstrating the potential of these ultrafast and green-synthesized MNPs.

2. Experimental

2.1. Reagents and materials

The salt precursor ferrous chloride tetrahydrate ($FeCl_2.4H_2O$) was purchased from Merck (Germany) and ferric chloride hexahydrate ($FeCl_3.6H_2O$), ammonia solution (NH_3, 30% and 25% v/v) and hydrogen peroxide (H_2O_2) were from Panreac Química (Spain). Citric acid anhydrous (ACS) used as coating agent was obtained from Fluka Analytical (USA). The coating agents such as dopamine (DA) hydrochloride ($C_8H_{11}NO_2$), mercaptopropionic (MPA) and isonipecotic (ISNPA) acids were purchased from Sigma-Aldrich (Germany). Sodium citrate (SC) tribasic dehydrate was acquired from Sigma-Aldrich (Spain), and chitosan (CS) was bought from Sigma-Aldrich (Portugal), while the horseradish peroxidase (HRP) enzyme, 2,2′-azino-bis(3-ethylbenzothiazoline-6-sulfonic acid) (ABTS) and mercury chloride ($HgCl_2$) were purchased from Sigma-Aldrich (USA), and N-Ethyl-N′-(3-dimethylaminopropyl) carbodiimide hydrochloride (EDAC) was purchased from Sigma-Aldrich (Japan). Ethanol and acetone for washing steps were purchased from Alcoholes del sur (Spain). The different solutions were prepared with nanopure water obtained from a Milli-Q system (18 MΩ·cm, Millipore, Bedford, MA).

The reagents for the immunoprecipitation study were tris-buffer from Fisher Scientific (China), sodium chloride (NaCl) from Merck (Germany), triton X-100 from Amresco (USA), sodium fluoride (NaF) from VWR International (Belgium), ethylenediaminetetraacetic acid (EDTA) ($C_{10}H_{16}N_2O_8$), sodium orthovanadate (Na_3VO_4) and protease inhibitor cocktail (PIC) from Sigma-Aldrich (USA). Ethylene glycol-bis-(β-aminoethyl ether)-*N′,N′,N′,N′*-tetraacetic acid (EGTA) and sodium dodecylsulfate (SDS) were from AppliChem (Germany), sodium pyrophosphate, β-glycerolphosphate (β-G-P), calyculin A, green fluorescent protein (GFP) antibody, actin, and glyceraldehyde 3-phosphate dehydrogenase (GAPDH) were from Santa Cruz (USA). Finally, the tribbles2 (TRIB2) antibody rabbit specie was provided by the National Oncologic Research Center (Spain) through the Department of Biomedical Sciences and Biomedicine (University of Algarve, Portugal).

2.2. Instrumentation

Magnetic nanoparticles were synthesized using a Q700 high energy ultrasound generator (QSonica Sonicators, Newtown, Connecticut, USA) equipped with a titanium tip of 13 mm that provides a maximum output power of 600 W. A Microtrac Nanotrac Wave particle analyser (Meerbusch, Germany) was employed to obtain routinely MNPs size distribution. This equipment is based on the dynamic light scattering (DLS) technique and uses a 3 mW (nominal power) laser diode emitting at a wavelength of 780 nm. The products were characterized in order to elucidate their composition, crystal structure, particle size, morphology and magnetization by X-ray Diffraction (D8 Advance-A25 Twin-twin, Bruker, USA), Fourier Transform Infrared Spectroscopy (IR Affinity-1S

WL, Shimadzu, Japan), Thermogravimetric analysis (TGA Q50 V20.13, TA Instruments, USA), Scanning and Transmission Electron Microscopy (Nova NanoSEM 450, FEI, ThermoFisher, USA and Talos F200X TEM Thermo Fisher Scientific, respectively), and vibrating sample magnetometry (Cryogenic Ltd., United Kingdom). A model V-650 UV/vis spectrophotometer (Jasco, Spain) was used to perform the corresponding measurements in the enzymatic inhibition study.

2.3. Synthesis

2.3.1. Magnetic iron oxides nanoparticles

Bare MNPs were synthesized using the co-precipitation method [35], enhanced with a high energy sonochemical probe. The initial sonochemical synthesis of MNPs consisted in a stoichiometric mixture of 0.005 mol (0.99 g) of $FeCl_2{\cdot}4H_2O$ and 0.01 mol (2.70 g) of $FeCl_3{\cdot}6H_20$, which were dissolved in 50 mL of Milli-Q water and kept under nitrogen atmosphere. The mixture was directly irradiated with the sonicator probe at a frequency of 20 kHz, operated at 50% (≈9300 J) of its total amplitude under nitrogen atmosphere in order to mix the salts solution. Afterwards, 4 mL of NH_3 solution were poured dropwise into the mixture producing an instant change in color. The ultrasound irradiation continued after the addition of the basic solution for 5 min. The black precipitate was washed with Milli-Q water using magnetic precipitation and decantation until a neutral pH was obtained. Finally, the black precipitate was further dried in an oven at 60 °C overnight. The total reaction time was 5 min; however, it was observed that the black precipitate was formed since minute 1 of reaction time. Thus, time was considered to be introduced in the DOE as well as amplitude, as described in the next subsection.

2.3.2. MNPs synthesis optimization by DOE

Response surface methodology (RSM), specifically, factorial design with 3 levels and 2 factors (3^2) was used to optimize the method and minimize the response variable (to obtain smaller particle sizes). Factors such as amplitude and time were considered to optimize the sonochemical synthesis of MNPs; three different levels were employed for each of them: 20%, 40%, and 60%; and 1, 3 and 5 min, respectively.

The quantities of the reagents were kept the same as described for the initial sonochemical synthesis of MNPs (see Section 2.3.1). Consequently, the mixed iron salt solution was placed in ice bath and moderate nitrogen atmosphere was applied for 1 min. Then, the iron salt solution was irradiated with the sonicator probe and 4 mL of NH_3 solution were immediately poured into the mixture within 10 s. An instant change in color was observed and a black precipitate formed. The applied amplitude and time were settled according to the different levels previously defined. The final temperature of each experience was kept within 30–38 °C. The black precipitate was cleaned with Milli-Q water applying an external magnetic field until the pH of the solution was neutral. Next, the MNPs were dried in an oven at 60 °C overnight. Finally, some dried MNPs were stored in 20 mL clear plastic containers at room temperature and some others redispersed in aqueous solution and stored at 4 °C.

2.4. Functionalization of MNPs with different coating agents

Three different methodologies were employed for the functionalization of bare MNPs. First, the PBS was sonicated to remove as much oxygen as possible before dissolving the dopamine avoiding its oxidation. To make a layer of polymerized dopamine or polydopamine (PDA) on the MNPs surface (PDA@MNPs), 500 mg of MNPs from synthesis with factors amplitude: 40% and time: 1 min, were dispersed in 25 mL of a 10 mM solution of dopamine, previously prepared in phosphate buffer solution (PBS 0.1 M at pH 8.5). The mixture was kept for three hours under continuous stirring at 60 rpm. Afterwards, the cleaning process was performed with PBS using magnetic precipitation and decantation to remove the excess of polydopamine. PDA@MNPs were dried for 5 days at 60 °C and carefully grinded.

The second methodology involves the use of chitosan (CS) to functionalize the MNPs. A 10 mM (42.3 mg) chitosan solution was prepared in 25 mL of water at pH 3 under magnetic stirring until complete dissolution. The pH was dropwise adjusted to 5.2 using NH3 (25% v/v). Once the pH was reached, 500 mg of bare MNPs (synthesis factors, amplitude: 40%; time: 1 min) were immediately added into the CS solution. The CS solution containing the MNPs was kept under magnetic stirring overnight. The cleaning process was carried out with distilled water until a neutral pH was reached. The CS@MNPs were dried at 60 °C for 5 days and carefully grinded.

Non-polymeric species ACS, MPA, ISNPA and SC were used for the third functionalization methodology. Carboxylate groups, obtained from these species, were anchored on the bare MNPs following a previously described methodology [36]. Bare MNPs (400 mg) from synthesis with factors of amplitude: 40% and time: 1 min were re-suspended in 55 mL of different acid solutions (0.02 g/mL, pH 5.2) of ACS, MPA, ISNPA and SC. The different mixtures were heated at 80 °C for 6 h using a reflux system. The black precipitates were washed with Milli-Q water (ISNPA@MNPs) and acetone (ACS, MPA@MNPs) three times. The coated MNPs were collected through magnetic precipitation and decantation, and further dried overnight at 60 °C. Finally, MNPs were carefully grinded and some dried MNPs were stored in 20 mL clear plastic containers at room temperature and some others redispersed in aqueous solution and stored at 4 °C.

2.5. Enzymatic inhibition study

Initially, the size was checked with DLS as a rapid screening technique to evaluate if MNPs were considered suitable for use. First, 2 mg of dried MNPs were redispersed in 10 mL of aqueous solution, ultrasound bath was applied for 2 min and after this short process, the size was assessed with DLS; then, the process continued as described below.

Interferences for PBS, hydrogen peroxide and MNPs were investigated in order to avoid overlapping with the ABTS spectrum. ABTS solution was daily prepared in PBS (0.1 M, pH 6) previously subjected to nitrogen stream for 10–15 min to remove the oxygen and avoid its oxidation. For this purpose, different concentrations of distinct components (see Table 1) were prepared in a total volume of 1.5 mL and further vortexed for 10 min. The absorbance was immediately measured in the 800–400 nm range.

Afterwards, HRP enzyme was attached on the surface of PDA@MNPs to carry out enzymatic inhibition studies. First, 50 mg of PDA@MNPs were dispersed in 2.5 mL in a HRP solution (0.5 mg/mL) prepared in PBS (0.1 M, pH 7.4) under gently stirring at room temperature for 3 h. Thereupon, the sample was cleaned using magnetic precipitation and decantation with PBS (pH 7.4) to remove the excess of unreactive enzyme. However, in this occasion the resultant product was redispersed in 1 mL of PBS (pH 7.4). This dispersion was kept at 4 °C and used within 2 weeks to avoid loss of enzymatic activity. Once the HRP/PDA@MNPs were prepared, the enzymatic inhibition study was carried out. Hg^{2+}

Table 1
Composition of solutions used to perform the Hg^{2+} calibration curve for the biosensing assay.

Species in the assay (μL)[a]	Blank	0.03 ppm Hg^{2+}	0.04 ppm Hg^{2+}	0.05 ppm Hg^{2+}	0.06 ppm Hg^{2+}
$HgCl_2$ (21 μg/mL-ppm)	–	2.9	3.8	4.83	5.80
PBS (0.1 M)	1027.5	1024.6	1023.7	1022.7	1021.7
HRP/PDA@MNPs (0.25 mg/mL)			7.5		
ABTS (0.3 mg/mL)			450		
H_2O_2 (0.3%v/v)			15		
Total volume (μL)			**1500**		

[a] Volume added (μL) of the corresponding species for each assay.

(0.060 ppm) was added to the mixture of ABTS, H_2O_2 and HRP/PDA@MNPs for a period of time of ten minutes. The measurements (n = 3) were performed in the absorbance mode from 800 to 400 nm.

2.6. Anchoring of antibody and immunoprecipitation studies

For immobilizing the antibody on the surface of the coated-MNPs (CA@MNPs), 5 mg of each CA@MNPs were dispersed in 500 mL of PBS (0.2 M at pH 5.6), and sonicated for 10 min. Then, 5 mg of N-ethyl-N′-(3-dimethylaminopropyl) carbodiimide hydrochloride (EDAC) were added into the previous solution. PDA@MNPs were dispersed in 500 mL of PBS 0.1 M at pH 7.4 and EDAC was not necessary.

Finally, 50 μL of the antibody solution were poured in the mixtures and kept under magnetic stirring at room temperature overnight. The same procedure was followed for a similar solution, but kept at 4 °C under mechanical movement with a nutating mixer. Afterwards, the mixture of antibodies and CA@MNPs (Ab/CA/@MNPs) was cleaned using magnetic precipitation and decantation with the proper PBS (0.2 M, pH 5.6 or 0.1 M, pH 7.4) in order to remove the excess of unreacted antibody.

The Ab/CA/@MNPs were re-dispersed in 1 mL of the corresponding PBS, which was kept at 4 °C to further prove the presence of the antibody on the surface of CA@MNPs before using them for the immunoprecipitation studies.

Immunoprecipitation was carried out using a whole cell protein lysate. Cells were lysed using an ice cold buffer (5% triton X-100, 1 M NaF, 0.5 M EDTA, 0.5 M EGTA, 200 mM sodium pyrophosphate, 1 M β-G-P, 100 mM Na_3VO_4, 0.1 mg/μL calyculin A and 0.1 mg/μL Protease inhibitor cocktail, S). The total amount of protein was calculated using the Bradford method and 20 uL were loaded in a 10% sodium dodecyl sulfate-polyacrylamide gel electrophoresis (SDS-PAGE) gel.

Once the antibody was attached to the CA@MNPs, two immunoassays took place using the Ab/SC@MNPs and Ab/PDA@MNPs. First, 200 μL of two different dispersed MNPs from a previous solution (5 mg/mL) were incubated overnight with two different protein extracts at two different concentrations (4 and 2 μg/mL) from U2OS parental and U2OS TRIB2-GFP isogenic cell lines.

U2OS refers to an osteosarcoma cell line with low TRIB2 expression levels and the U2OS TRIB2-GFP counterpart expresses TRIB2 fused with GFP. The mixture was separated through precipitation and decantation applying an external magnetic field, in order to resolve and analyze each of the separated fractions using SDS-PAGE and western blot.

The immunoprecipitations (IPs) were performed separately for each of the different coated-MNPs and for the different protein concentrations [37]. Additionally to the immunoprecipitated fraction, flow through (FT) and whole extract (WE) fractions were collected as a control for each of the three IPs. GFP antibody was used as an alternative antibody to detect TRIB2 presence, ACTIN and GAPDH were used as loading controls.

3. Results and discussion

3.1. Optimization of the synthesis parameters of MNPs obtained using a sonochemical method

The current synthesis based on a co-precipitation methodology and further enhanced with high energy ultrasound provides a unique medium in which reactions take place more effectively than other previous reported iron oxides MNPs sonochemical synthesis [29,30]. This was positively confirmed through several syntheses within the current research, and through the proper data treatment with DOE. It was possible to reduce the amount of employed reagents keeping low costs of production and protecting the environment. Furthermore, the applied energy (2826 J), was minimized and the reaction time was drastically reduced to one single minute obtaining superparamagnetic iron oxide-based MNPs. Mean particle size distributions were 11 ± 2 nm and Ms. values between 56 and 66 emu/g according to predefined factors which will be discussed in the next subsection. The high yields of the obtained product were above 90%, which is also remarkable.

3.1.1. Experimental results derived from experimental design

A high-energy ultrasound generator, equipped with a titanium tip, was used as energy source, since it allows a better control on amplitude (energy) than the typical co-precipitation method using an ultrasonic bath [38] (not focalized energy and much dissipation) or heating [39] (much loss of energy), in which controlling delivered energy and temperature over time is complex. The device used in the present research supplies itself the necessary power (amplitude) in the set time, and temperature was controlled between 30 and 38 °C during the entire process with an ice bath.

Based on the RSM, 3^2 factorial design for two independent factors (amplitude and time), 18 experimental syntheses were performed. The design implied 9 experiments in duplicate and randomly carried out to eliminate any potential source of error. The obtained MNPs from the 18 syntheses were assessed by dynamic light scattering (DLS), which has been demonstrated to be a useful technique for this purpose (immediate and routine analysis) [26]. The size distributions showed Gaussian shape; however, the weighted mean of the hydrodynamic radius was used [size(nm)].

MNPs sizes ranging from 33 to 60 nm were obtained, as observed in Table 2. The three highest mean values for particle size were obtained for experiments 1 (58 nm), 3 (60 nm) and 8 (53 nm). On the other hand, the smallest mean values were obtained for exp. 9 (33 nm) and 4 (36 nm).

Experiments 1 and 4 were carried out with an amplitude of 60%, but setting up different time (5 and 1 min, respectively). The mean particle size and relative standard deviation (RSD) were higher in exp. 1 (58 nm and 8.6%) than in exp. 4 (36 nm and 7.9%). This difference on nanoparticle sizes is attributed to the high applied energy and extended times. This fact was also supported with experiment 6 (A: 60% (6927 J), t: 3 min) where a mean particle size of 42 nm and RSD of 17% were obtained. This behavior is the result of high temperatures generated by the applied amplitude through extended periods of time. As previously elucidated, elevation of temperature, generated by the cavitation phenomenon, promotes the formation of bigger MNPs since it affects the nucleation and growth process in the nanoparticles formation produced with classical co-precipitation [40,41].

Experiments 2, 5, 7 and 9 had a reproducibility of 4% in terms of RSD using amplitude values of 20% and 40%, for exps. 2 and 5, and for exps.

Table 2
Results of design of experiments (DOE).

Experiment	Experimental parameters		Replicate 1 (size, nm)	Replicate 2 (size, nm)	x ± SD (nm)	% RSD
	Amplitude (%; Joules)	Time (min)				
1	60; 15,219	5	61	54	58 ± 4.9	8.6
2	20; 1740	1	47	50	49 ± 2.1	4.4
3	40; 6997	3	63	57	60 ± 4.2	7.1
4	60; 3068	1	34	38	36 ± 2.8	7.9
5	20; 8530	5	40	38	39 ± 1.4	3.6
6	60; 6927	3	37	47	42 ± 7.0	16.8
7	40; 9257	5	37	39	38 ± 1.4	3.7
8	20; 15,219	3	49	56	53 ± 4.9	9.4
9	40; 2826	1	34	32	33 ± 1.4	4.3

7 and 9, respectively. This supports the fact that high amplitude values increase RSD values during the sonochemical syntheses.

Therefore, with the current approach based on high energy ultrasound, it was possible to prove that the particle sizes were small and uniformly distributed using low amplitudes and short reaction times.

3.1.2. Statistical analysis of results

DOE allows comparing the effect of two or more factors in the outcome of an experiment, as well as the effect of each factor separately. When effects are compared with more than one factor, interaction between the analyzed factors takes place if results are statistically different [42,43].

The analysis of variance (ANOVA) was performed at a significance level of 95%. The results of ANOVA are represented in a Pareto diagram (see Fig. S1 from Supplementary Material) that shows the standardized effects of the principal factors and their interactions from the most to the less important factor. A t-value of 2.0796 was established (vertical line in the standardized Pareto diagram) to evaluate which of them are statistically significant. ANOVA results verified that the interaction between amplitude and time, and the quadratic interaction of time influenced the most over the particle size. ANOVA allowed calculating the adjustment of the mathematical model generated from the experimental data, where 86.07% of the system total variance was explained by the mathematical model generated from the variance of the factors. The present research was performed to obtain one response (R_1), which was to minimize the particle size. According to the experimental data of this response, the regression equation was presented to predict the relationship of response value and the amount of defined factors. The fitted model on the particle size of samples can be expressed as follows:

The optimum calculated values for amplitude and time from this equation were 50.50% and 1 min, respectively.

$$R_1\ [\text{Particle size}, nm] = 54.625 - 1.51875\ [\text{amplitude}] + 16.9167\ [\text{time}] + 0.013125\ [\text{amplitude*amplitude}] + 0.19375\ [\text{amplitude*time}] - 3.875\ [\text{time*time}]$$

In this regard, the independent main effects presented by amplitude and time were also studied (see Fig. S2 from Supplementary Material) observing two different profiles. The particle size is represented on the Y axis and each of the different tested values for amplitude and time on the X axis. The right negative parable on Fig. S2 indicates that one minute of reaction time produces smaller particle size than five minutes. The left positive parable refers to the different amplitude values used in the syntheses, which indicates that a high value of amplitude produces bigger MNPs particle size.

Nonetheless, observing the center of the left parable of amplitude, it was detected that the particle size could be decreased using a lower value of amplitude. Hence, it was decided to study the interaction among amplitude and time (see Fig. S3 from Supplementary Material). Fig. S3 represents the interaction plot of amplitude and time where the estimated profile of response is obtained for minimum and maximum time values, over the range of amplitude values. This figure confirms that 5 min of reaction time had a continuous and increasing important effect over the particle size as amplitude was elevated. On the other hand, high amplitude values around 50% (3172 J) for one minute seemed to provide smaller particle sizes, but as the amplitude decreases the particle size increases. Additionally, it is noteworthy to observe the intersection point between amplitude values around 35 to 40, which may indicate that the optimum amplitude value is around this range. Thus, extra syntheses with amplitude at 50% were performed; the resulting MNPs were also characterized in order to compare them with the previous sonochemical synthesis. The discussion of these results is described in Sections 3.2.1 and 3.2.2.

3.2. Characterization of MNPs

3.2.1. Scanning electron microscopy (SEM)

SEM images of the different bare MNPs synthesized under several amplitude values were performed. The different synthesis micrographs and histograms with their statistical charts (*N*: number of counted particles, *x*: average size of the population and *SD*: standard deviation) are displayed on Fig. 1. In order to have more accurate results, the obtained statistics from the SEM images were performed with >100 counts of MNPs using the Digital Micrograph software (Gatan Inc., USA).

Spherical and well-defined MNPs are observed from SEM images on Fig. 1(A.1, B.1 and C.1), which were obtained after 1 min of irradiation and 40%, 50% and 60% of amplitude, respectively. The obtained mean particle size and size distribution can be considered the same, as observed in Fig. 1(A.2, B.2 and C.2). Thus, it is demonstrated that MNPs with size around 13 ± 3 nm can be reproducibly synthesized with amplitudes values of 40%, 50% and 60% and 1 min of reaction time.

Nonetheless, an amplitude value of 40%, from Fig. 1(A.1), was chosen for future syntheses, since its Gaussian distribution was mainly centered on 12 to 13 nm (the lowest average size value) and it generated the least amount of energy (2826 J), while synthesis with amplitude values of 50% and 60% and 1 min generated 3071 J and 3068 J of energy, respectively.

Bare MNPs synthesized with amplitude 40% and time 1 min were functionalized with PDA, ACS, ISNPA and MPA. Such MNPs were analyzed with SEM to assess the size increment. Images, histograms and statistical charts are shown in Fig. 2. SEM images from Fig. 2(A.1, B.1 and C.1) reveal well defined, spherical and bigger MNPs, due to their coating layer, as can be seen in the histograms from Fig. 2(A.2, B.2 and C.2), which present slightly higher mean particle sizes for the functionalized MNPs. The presence of the coating layer is expected to lead to higher stability of the MNPs, due to the functional groups linked on their surface.

In summary, it was found out through electron microscopy that reproducible MNPs can be synthesized using the studied amplitudes values of 40%, 50% and 60% with 1 min of reaction time. Additionally, the presence of the coating agents was properly confirmed, since there was an increment of the initial particle size of bare MNPs. Finally, it was demonstrated that the enhanced green and ultrafast method of synthesis aided by high energy ultrasound and DOE, possesses interesting and useful advantages, mainly related to reproducibility and significantly save time and lower production cost.

3.2.2. Transmission electron microscopy (TEM)

Bare MNPs and PDA@MNPs were analyzed using TEM. As it can be seen from Table 3, MNPs possess an average size about 11 ± 2 nm, being >90% of the particles with a size between 8 and 16 nm. For PDA@MNPs, the obtained size and the distribution data are similar; however, a carbon-containing film coming in this case from the PDA covering, seems to coat agglomerated MNPs, as discussed below.

The first analyzed sample was bare MNPs. High resolution electron microscopy (HREM) image of bare MNPs on Fig. 3(A) displays their planar distance, which was about 2.99 Å. Moreover, the Digital Diffraction Patterns (DDP), built from the previous HREM image, allowed to corroborate the composition of the magnetic nanoparticles. The distance between planes (interplanar spacing) in the reciprocal lattice was about 2.40 Å and 3.385 Å for planes [222] and [220], respectively, as seen in Fig. 3(B), which are very close to the typical

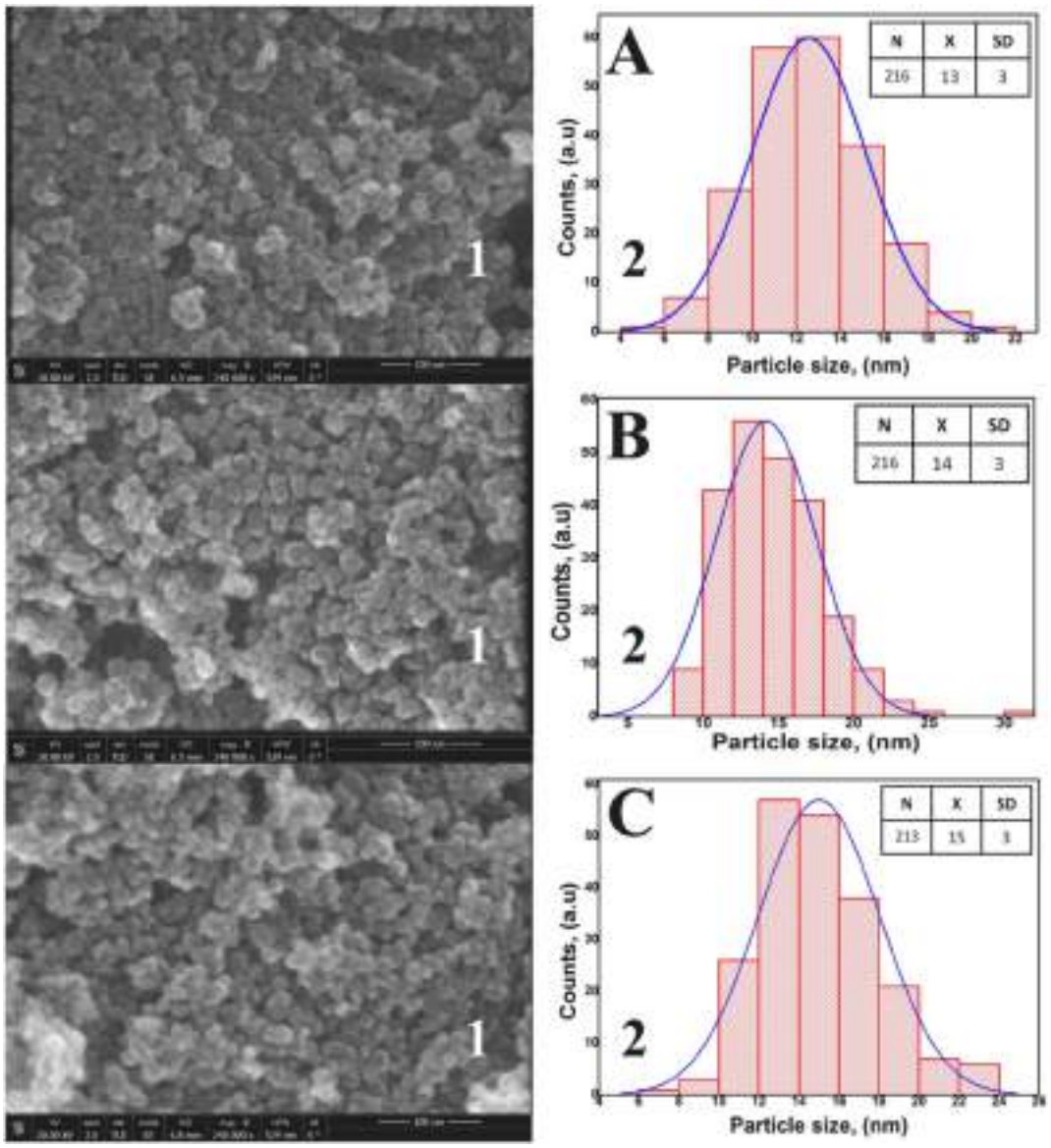

Fig. 1. Scanning electron microscopy (SEM) images of magnetic nanoparticles (MNPs) synthesized at different values of amplitude and 1 min of time. A.1) 40% B.1) 50% and C.1) 60%. Corresponding histograms and statistical charts are shown for each of them in A.2), B.2) and C.2), respectively. (N: counts, X: average size, SD: standard deviation).

planes of magnetite phase (Fe_3O_4) [44]. The high-angle annular dark-field (HAADF) image in Fig. 3(C) represents a MNPs cluster, whose compositional mapping is shown in Fig. 3(D). In this map, the green dots represent oxygen atoms, while iron atoms can be seen as red dots. As can be observed from both images, they can be clearly overlapped, corroborating the composition of the MNPs. The composition of the sample was studied with X-ray energy-dispersive spectroscopy (EDS) analyses, as displayed in Fig. 3(E). Carbon, copper, oxygen and iron were found; the former two associated to the grid, and the latter two to the iron oxide sample.

Subsequently, PDA@MNPs were analyzed with TEM. The micrograph at HREM mode was taken first, and consequently the DDP was built from the previous micrograph. The measured planar distance from the HREM image was about 2.94 Å, represented by Fig. 4(A). The interplanar spacing was about 3.388 Å for plane [220] as observed in Fig. 4(B), which is very close to the planar distance of 2.97 Å corresponding to the [220] family planes of face-centered cubic (FCC) crystals from magnetite phase (Fe_3O_4) [45]. The HAADF image on Fig. 4(C) reveals a MNPs cluster, whose compositional mapping is reported in Fig. 4(D). Fig. 4(C) and (D) can be clearly overlapped, corroborating the composition of the MNPs. In the compositional mapping of PDA@MNPs (Fig. 4(D)), the green dots represent oxygen atoms, while iron atoms can be seen as red dots and carbon atoms as blue dots. The origin of carbon atoms could be attributed to the added PDA cover, since the amount of carbon (semi-quantitatively) is higher in PDA@MNPs than in bare MNPs, as observed in the respective EDS spectra of PDA@MNPs, represented by Figs. 3(E) and 4(E). Nonetheless, the mean particle size was similar in both cases, since the measured value of the carbon-containing film that surrounds the agglomerated MNPs is not included, but clearly observed in PDA@MNPs (Fig. 4(A)) when compared to bare MNPs (Fig. 3(A)).

3.2.3. X-ray diffraction (XRD)

The crystalline arrangement of bare MNPs, PDA@MNPs, ACS@MNPs, MPA@MNPs, and ISNPA@MNPs was characterized by XRD, as can be appreciated in Fig. 5(A). The diffraction peaks reflect the magnetic crystal as a cubic inverse spinel structure with oxygen forming a face-centered cubic (FCC) structure and iron cations occupying

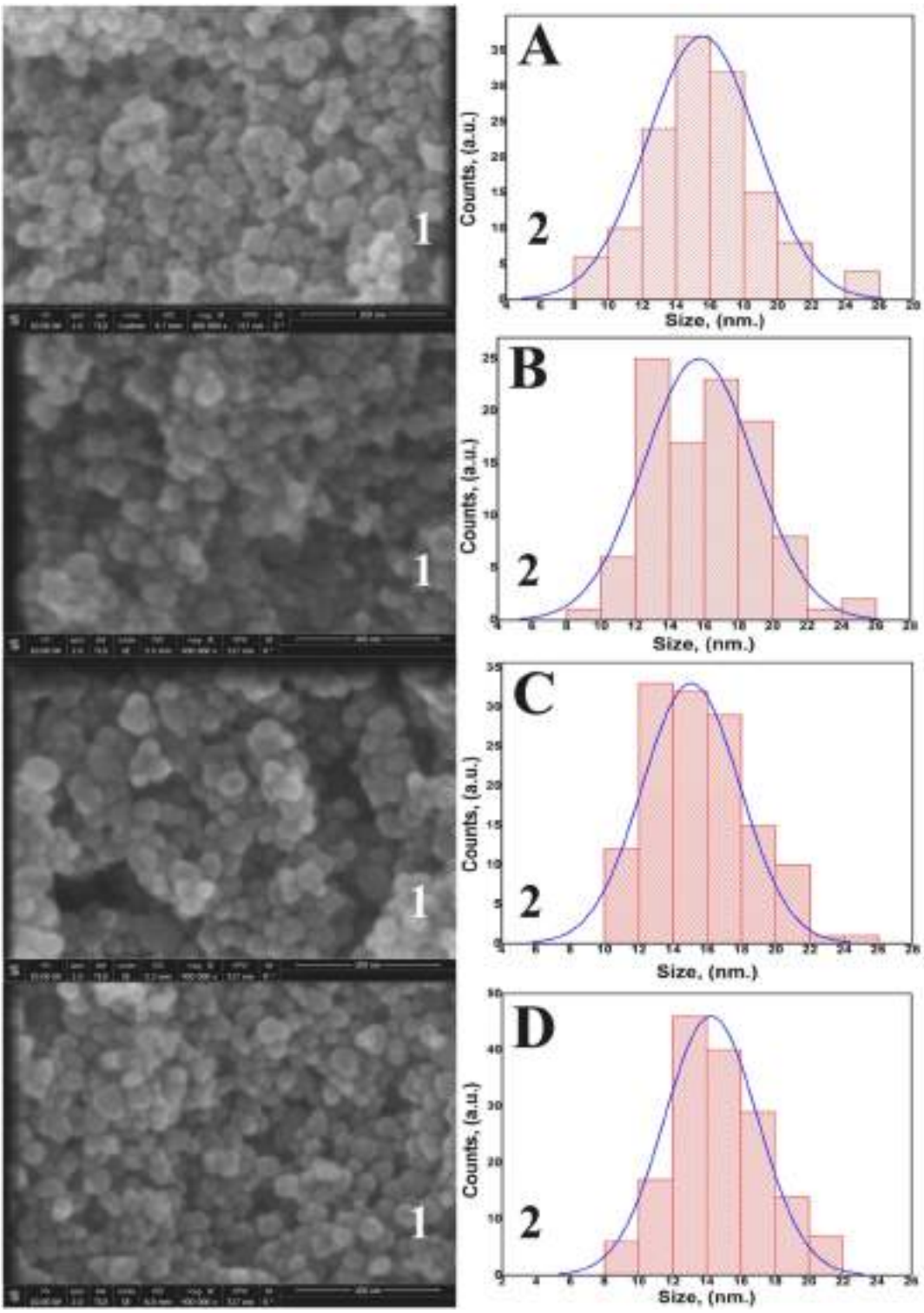

Fig. 2. SEM images of different functionalized MNPs synthesized at amplitude 40% and 1 min of time. A.1) polydopamine (PDA)@MNPs, B.1) citric acid (ACS)@MNPs, C.1) mercaptopropionic acid (MPA)@MNPs, and D.1) isonipecotic acid (ISNPA)@MNPs. Corresponding histograms and statistical charts are shown for each of them in A.2), B.2), C.2) and D.2), respectively. (N: counts, X: average size, SD: standard deviation).

tetrahedral and octahedral sites [16], which match well with those of the bulk Fe_3O_4. (JCPDS card No. 88-0315, 2002). However, this is not a conclusive result on the presence of pure magnetite, since the diffraction peaks for maghemite phase appear at similar 2θ angles. Nonetheless, the presence of other iron oxides, such as hematite, if exists, is under 5%.

The nanocrystallite size was also estimated using Scherrer equation, taking into account the correction for the width of the diffraction maxima due to the equipment. The sizes were calculated from the most intense reflections (Bragg angle, $2\theta \approx 35.5^{\circ}$) obtaining diameter sizes of 13, 14, 15, 14 and 13 nm for bare MNPs, PDA@MNPs, ACS@MNPs, MPA@MNPs and ISNPA@MNPs, respectively. The calculated diameters were almost the same to those obtained from SEM analyses. In fact, the same value was obtained for bare MNPs suggesting a predominant monocrystalline structure for the synthesized MNPs.

Table 3
Particle sizes obtained from TEM analysis.

MNPs	Mean size (nm)	SD (nm)	Distribution range (nm)	Range with more %	Variance of sample %
Bare MNPs	11	2	7–16	8–15 (94%)	4.23
PDA@MNPs	11	2	6–20	8–16 (94%)	6.05

3.2.4. Fourier transform infrared (FTIR) spectroscopy

FTIR absorption spectra were performed to investigate the composition of the synthesized nanoparticles and to detect the functional groups from the organic species after their anchoring to bare MNPs surface. Fig. 5(B) exposes the FTIR spectrum of bare MNPs, where a broad band can be observed in the zone of low frequencies (around 600 cm^{-1}) associated with the characteristic vibrations of Fe—O (570–600 cm^{-1}) [2,45,46]. It is noteworthy the splitting-up of this peak which is attributed to the symmetry degeneration on the octahedral B sites and the split of the energy levels of the MNPs [46].

Moreover, the bands appearing at 3433 and 1629 cm^{-1} are ascribed to the stretching and bending vibrations of the surface hydroxyl groups and adsorbed water molecules [38], respectively. The PDA@MNPs spectrum still shows the characteristic broad band of MNPs at 600 cm^{-1}. This spectrum shows a band at 1047 cm^{-1} assigned to the ring breathing of ortho-disubstituted benzene rings, while the bands at 1490 and 1630 cm^{-1} are considered to be present due to the indoline structure of the polydopamine [47]. Nonetheless, the spectrum of CS@MNPs is not displayed because it only had the bands of the MNPs, suggesting that CS either was not attached to their surface or it was but to a very small extent, so its bands were not strong enough to be seen.

The FTIR spectra of coated MNPs with the molecules containing carboxylic groups are also represented in Fig. 5(B). Two bands around 1400–1420 and 1580–1600 cm^{-1} can be appreciated in all the cases, which can be designated to the specific symmetric and asymmetric stretching vibrations of the carboxylate group (COO^{-}) [48], respectively. However, in the spectra of ACS and MPA there is a small band at 1713 cm^{-1} attributed to the presence of some protonated carboxylic groups (COOH), since the pKa values of ACS are 3.13, 4.76 and 6.40, and that of MPA is 4.34. The final pH of the solutions, where the functionalization was performed, were 5.4 and 5.2, respectively. The coating agents were adsorbed on the surface of the MNPs and the characteristic broad band of MNPs is kept in the zone of low frequencies, demonstrating that the functionalization step did not modify the composition of the particles.

3.2.5. Thermogravimetric analysis (TGA)

In order to confirm the coating process of the MNPs, thermogravimetric analyses were performed and measured by percentage mass loss as temperature increased. The mass losses occurred within the temperature range of 100–400 °C, where some effects take place, such as decomposition of physisorbed (120–300 °C) and chemisorbed (>440 °C) coating agents on the surface of the MNPs [49].

Bare MNPs around 13 ± 3 nm, had a mass loss of 4%, mainly attributed to desorption of water molecules within the crystallite structure [50], as observed in Fig. 5(C). Thus, larger mass losses for the coated MNPs were expected, according to SEM and X-ray results.

In this context, ACS@MNPs presented a mass loss of 21%, which confirms the proper functionalization of MNPs with this coating agent. Being the highest mass loss observed fits well with the highest size found for these particles (16 and 15 nm, as obtained by SEM and XRD, respectively). The same was observed for MPA@MNPs but to a lesser extent. MPA@MNPs presented a mass loss about 9%, which is attributed to the covering agent. The mass loss was less than the obtained for ACS@MNPs as well as the particle size (SEM 15 nm, XRD 14 nm). The mass loss for ISNPA@MNPs was of 6%, which agrees with the particle size of 14 nm obtained by SEM. Finally, a mass loss similar to that of ACS@MNPs was expected for PDA@MNPs, since their particle sizes after the functionalization were the same (see Fig. 2A.2 and B.2). However, PDA@MNPs had a mass loss of 6%. According to the literature, this behavior could be attributed to the high porosity of such coating agent, producing coating layers with large thickness and high porosity [51].

3.2.6. Vibrating sample magnetometry analysis (VSM)

The superparamagnetic behavior of magnetic iron oxide nanoparticles is characterized by their singular hysteresis loops and by the zero value of their remaining magnetization and coercive field, which depend on the applied magnetic field. The saturation magnetization (Ms) value is an indicator of the complete magnetization of a sample, being around 90 and 74 emu/g for bulk magnetite and maghemite, respectively [52].

In this sense, the superparamagnetism of bare and functionalized MNPs is demonstrated in Fig. 5(D). All hysteresis loops pass through zero, indicating a zero coercive field and zero remaining magnetization. Furthermore, for all curves the ascending section coincides with the descending one, culminating with an area of zero for all the hysteresis loops of the samples. Additionally, the Ms value obtained for bare MNPs was 65.35 emu/g, for PDA@MNPs was 61.33 emu/g, for ACS@MNPs was 56.27 emu/g, for MPA@MNPs was 65.96 emu/g, and for ISNPA@MNPs was 65.43 emu/g, confirming their superparamagnetic behavior.

The results indicate that all of the Ms values are smaller than the Ms value for both bulk magnetite and maghemite. However, the Ms value increases as the mean particle size increases as well [53]. Thus, lower Ms values were expected for the current analyzed samples, since their mean particle sizes are 11 ± 2 nm. Additionally, the coating layers might decline the surface momentum contributing to contract the magnetic momentum of the MNPs [54]. Nevertheless, from these considerations, it is not possible to establish unequivocally the iron oxide phase (spinel type) present in these samples. On the other hand, the Ms values can be directly correlated and compared with SEM and TGA results. From this comparison, it is noteworthy to observe that the Ms values of MPA@MNPs and ISNPA@MNPs are just above (0.61 and 0.08 emu/g, respectively) the Ms value of bare MNPs when it should be the opposite. Nonetheless, this can be explained by virtue of their small increment of particle size (MPA@MNPs: 1 nm, and ISNPA@MNPs: 2 nm) and their small coating, what led to a minimum mass loss percentage (MPA@MNPs: 9%, and ISNPA@MNPs: 6%).

In this sense, the outcomes of the proposed synthesis based on high energy ultrasound are outstanding, obtaining small MNPs with good superparamagnetic behavior, which is an important feature for some applications where this behavior is highly required, such as magnetic resonance imaging (MRI).

3.3. Application of MNPs for biosensing

The obtained and further functionalized MNPs were employed in the field of biosensors, specifically one based on the enzymatic inhibition of horse radish peroxidase (HRP) caused by Hg^{2+}, following a completely distinct strategy from the one used by a different research group [55], which employed a similar system to directly detect H_2O_2.

The compound 2,2′-azino-bis(3-ethylbenzothiazoline-6-sulfonic acid) (ABTS) which, in the presence of hydrogen peroxide, undergoes oxidation to the ABTS radical, was used as a probe for enzymatic activity, since it can be quantified within the wavelength range of 400 to 800 nm. The UV–Vis spectra of all the compounds are shown in Fig. 6 (A). Neither PBS nor H2O2 did influence the total absorbance. The concentration of the MNPs was 0.25 mg/mL in order to avoid interferences, keeping a significant concentration of enzyme on its surface; thus, MNPs proved to be stable and possibly useful for the biosensing

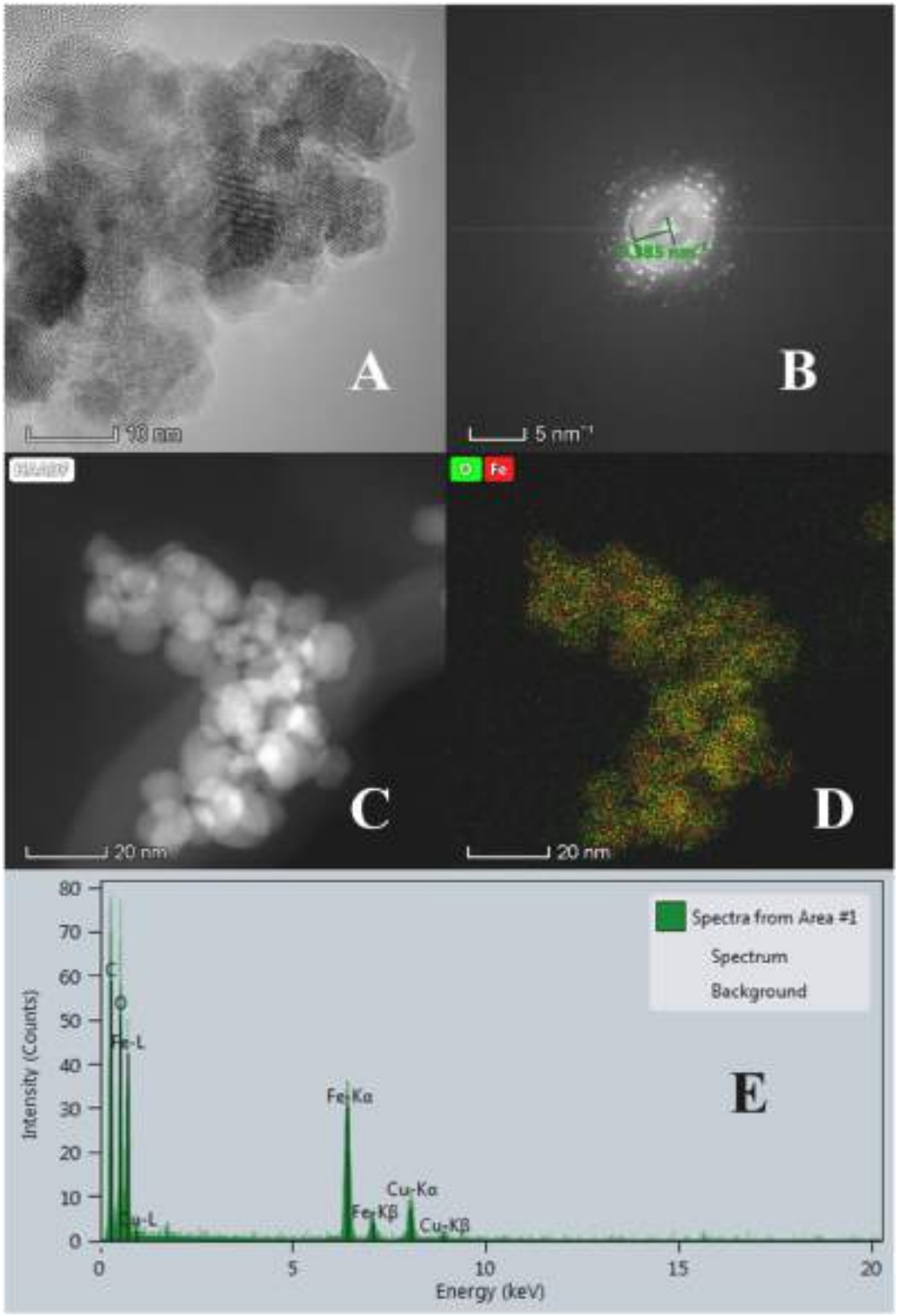

Fig. 3. Transmission electron microscopy (TEM) analysis of bare MNPs. A) TEM micrograph of MNPs taken at high resolution electron microscopy (HREM) mode, B) Digital Diffraction Pattern (DDP) built from A. C) TEM micrograph of a MNPs cluster taken at high-angle annular dark-field imaging (HAADF) mode, D) Compositional mapping from image C, and E) energy-dispersive X-ray spectroscopy (EDS) spectrum of image in micrograph C.

application. On the other hand, the concentration of ABTS was 0.3 mg/mL to maintain the absorbance value within the linearity. The absorbance spectrum of ABTS shows two main peaks at 417 and 736 nm, as shown in Fig. 6(A).

Fig. 6(B) lays out an intense signal on the absorbance (light blue line) due to the presence of the product of ABTS oxidation by H_2O_2 generated by the enzyme. When in presence of Hg^{2+}, the solution absorbance is lower (dark blue line), indicating a smaller concentration of the ABTS radical under these. This presents an evidence that Hg^{2+} affects the reaction, indicating that this harmful metal is a horseradish peroxidase

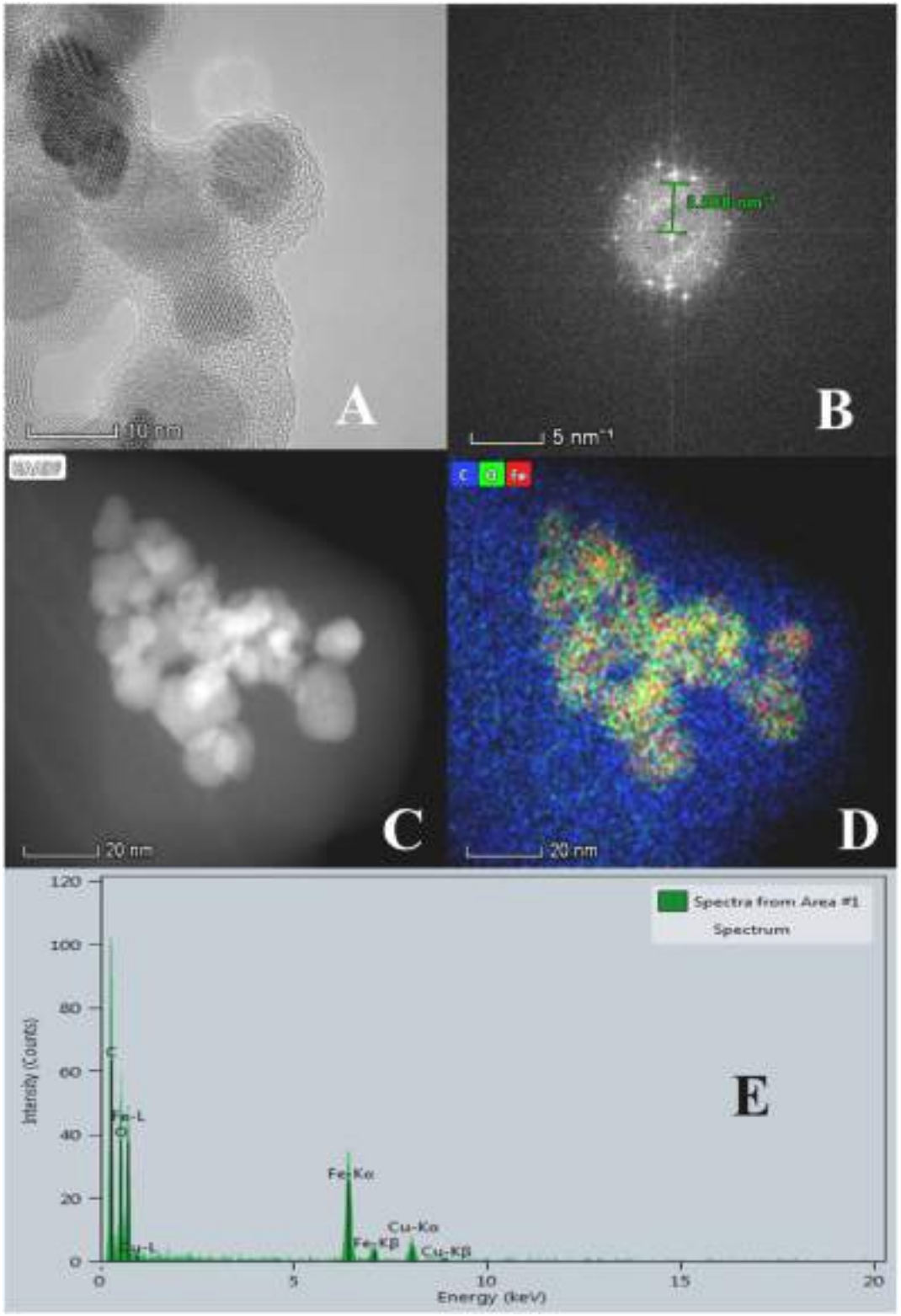

Fig. 4. Transmission electron microscopy (TEM) analysis of polydopamine (PDA)@MNPs. A) TEM micrograph of PDA@MNPs taken at HREM mode, B) Digital Diffraction Pattern (DDP) built from A, C) TEM micrograph of a MNPs cluster taken at HAADF mode, D) Compositional mapping from image C and E) EDS spectrum of image in micrograph C.

enzyme inhibitor, which irreversibly and significantly reduces its catalytic activity. (For interpretation of the references to colour in this figure legend, the reader is referred to the web version of this article.)

Different absorbance measurements were carried out at 417 nm to elaborate a calibration curve (Fig. 6(C)), according to Table 1. The calibration curve presented a correlation coefficient (R^2) of 0.9936, indicating an excellent linear fitting. The limits of detection and quantification (LOD = 3 *s/m* and LOQ = 10 *s/m*, *s*-standard deviation of the blank, *m*-slope of the calibration curve) were also calculated. A LOD = 0.004 ppm and LOQ = 0.013 ppm were obtained, where the former is

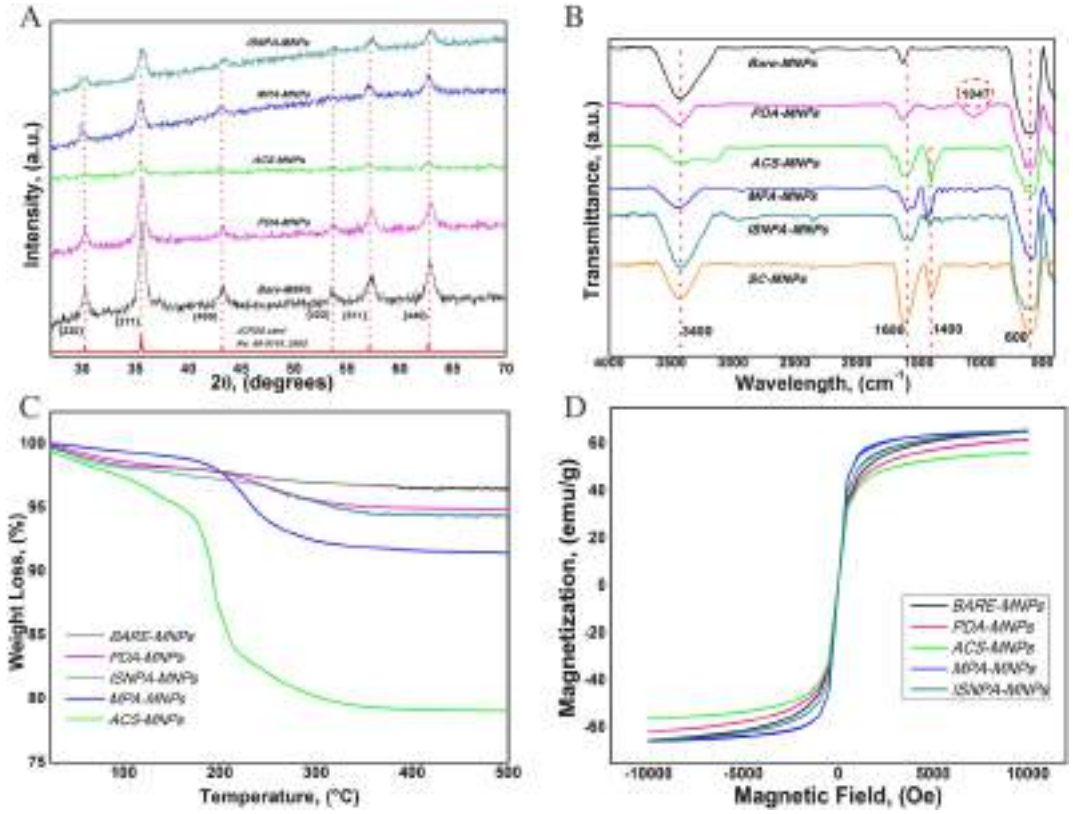

Fig. 5. Different characterization results for bare and coated MNPs (polydopamine, (PDA), citric acid (ACS), mercaptopropionic acid (MPA), isonipecotic acid (ISNPA)@MNPs), and sodium citrate (SC@MNPs) employing: (A) X-ray diffraction analysis, (B) Fourier transform infrared spectroscopy, (C) Thermogravimetric analysis, and (D) Vibrating sample magnetometer analysis.

close to the official limit according to EPA (0.002 ppm). Therefore, the bioanalytical application of synthesized nanoparticles is demonstrated.

3.4. Application of MNPs for immunoprecipitation

Immunoprecipitation (IP) is one of the most useful immunological techniques in which the presence and quantity of an antigen, the relative molecular weight of a polypeptide chain, its synthesis and degradation, and the interaction with proteins, nucleic acids or other ligands can be determined. In this study, two different IP assays were carried out using human U2OS osteosarcoma cells that have been manipulated to over-express TRIB2 protein coupled to a Green Fluorescent Protein (GFP) on the N-terminus, as well as a parental cell line which did not expressed exogenous TRIB2 protein. TRIB2 is a pseudokinase protein with oncogenic activity in melanoma [56,57] and has been shown to confer therapy resistance [58]. IP analysis of TRIB2 is an important approach to characterize its role in healthy and diseased cells.

3.4.1. Binding evaluation between CA@MNPs and antibodies

Bare and functionalized MNPs (CA@MNPs) were used in biomedical studies as a base tool to anchor a specific anti-TRIB2 antibody. Dried MNPs stored for three weeks at room temperature showed to be stable since they displayed antibody binding, as noted in Fig. S4 (see Supplementary Material, Fig. S4(A, B, C, D, and E)). The first lanes in both panels (left and right) show the specific band for the anti-TRIB2 polyclonal antibody while lane 2 refers to MNPs in the absence of antibody (negative control). Lane 3 and 4 represent the band of the polyclonal antibody attached at different temperature over different CA@MNPs.

Lane 1 of Fig. S4 has an intense band between 60 and 72 kDa; thus, bands in lanes 3 and 4, which are visible at the same level, were attributed to the antibody. Nonetheless, bands in lane 3 are more intense than those in lane 4. This difference in intensity indicated that more antibodies were able to bind on the surface of the MNPs at room temperature compared with the binding process at 4 °C; the same behavior was present in all evaluations. Interestingly, the TRIB2 antibody was attached on the surface of bare MNPs without any coating agent, as shown in Fig. S4 (E). This was probably due to the presence of negatively charged hydroxyl groups on the surface of bare MNPs, which can interact with positive areas of the antibody. However, the amount of attached antibody on the coated SC@MNPs, for example, was more intense than the amount of attached antibody on the uncoated ones, indicating that the coating agents significantly favor the attachment of the antibody to the MNPs.

It was demonstrated that this polyclonal antibody is stable and specific against TRIB2, and binds better to CA@MNPs at room temperature than to uncoated MNPs at 4 °C. For this reason, the following IP experiments were performed with Ab/CA@MNPs obtained at room temperature.

3.4.2. Immunoprecipitation reactions results

The immunoassays were performed with SC@MNPs and PDA@MNPs, the results are shown in Fig. 7. The first experiment was carried out employing SC@MNPs coupled with the antibody (Ab) (Ab/SC@MNPs) and a protein solution of 4 μg/mL. The second experiment was conducted using Ab/PDA@MNPs.

SC@MNPs were taken as representative sample of the other MNPs coated with organic acids and PDA@MNPs were used to compare their utility in both biosensing and immunoprecipitation applications. The immune complexes were denatured and resolved using SDS-PAGE and further analyzed with western blot as described before [59].

Fig. 7 displays the outcome of the two experiments including two immunoprecipitations (IP), flow through (FT) and whole extract (WE). IPs in Fig. 7A and B show the expected bands at 72 kDa which are clearly visible. Due to the different concentration in the initial protein solution,

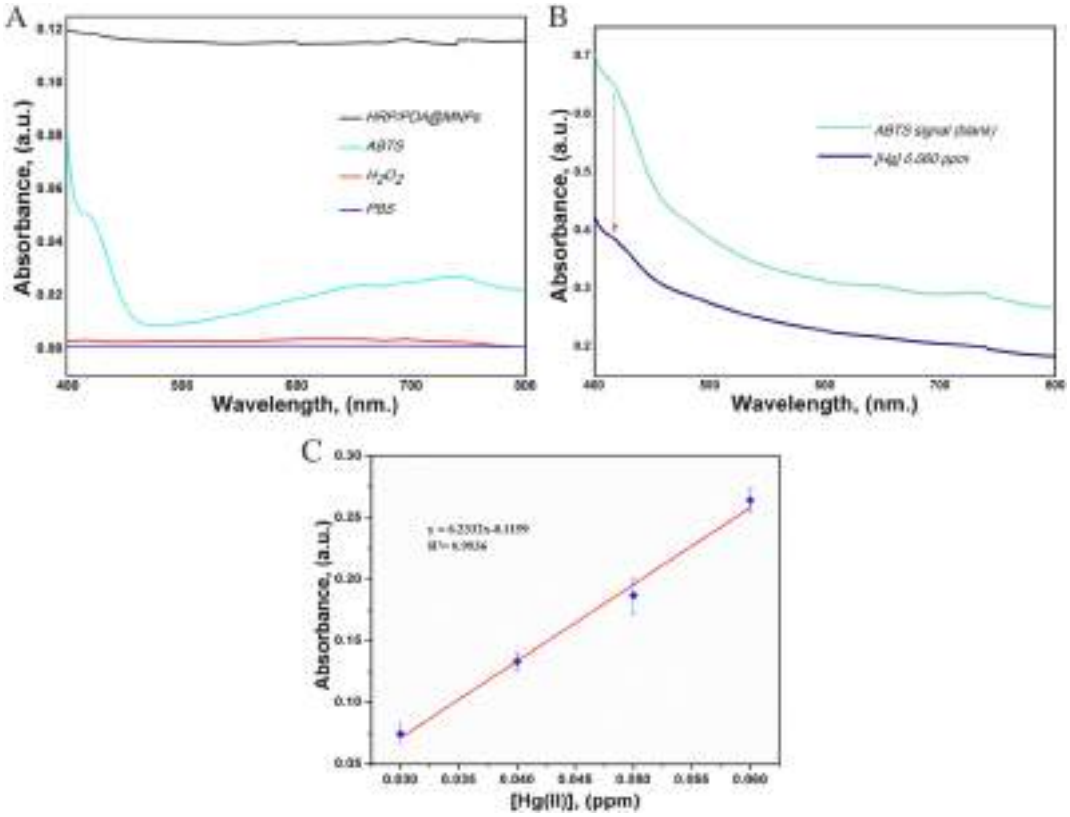

Fig. 6. (A) Absorbance spectra of different components ([horseradish peroxidase/polydopamine (HRP/PDA)@MNPs]: 0.25 mg/mL, [ABTS]: 0.3 mg/mL, [hydrogen peroxide (H_2O_2)]: 0.3% v/v, and [phosphate buffer solution (PBS)]: 0.1 M at pH 6. (B) Reduction of the ABTS signal due to irreversible inhibition of HRP enzyme by mercury. (C) Calibration curve built from the enzymatic inhibition study, measuring absorbance (n = 3) at wavelength 417 nm.

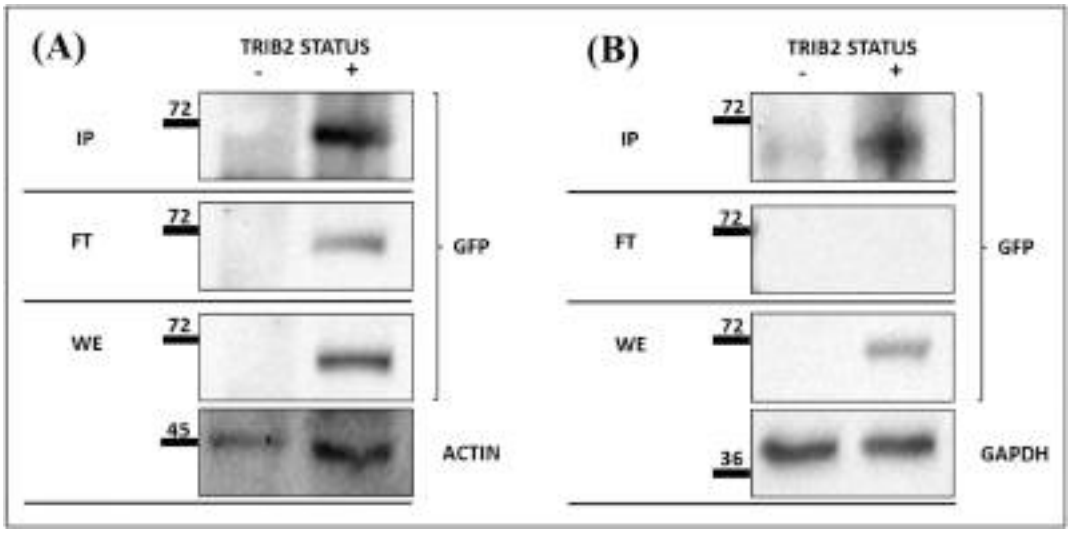

Fig. 7. Results of the immunoprecipitation-western blot (IP-WB) assays for two independent immunoprecipitation experiments employing different coated MNPs ((A) antibody/ sodium citrate (Ab/SC)@MNPs, and (B) Ab/polydopamine(PDA)@MNPs. Two different cell lines were tested (U2OS parental and TRIB2-GFP). Three primary antibodies (GFP, Actin and GAPDH) and three fractions were evaluated ("IP": immunoprecipitation, "FT": flow through, and "WE": whole extract. The GFP signal was at 72 kDa while the signal of actin and GAPDH were at 45 and 36 kDa, respectively. Both IPs A and B correctly detected the target protein.

the detected band of the immunoprecipitated fusion protein against GFP is more intense in Fig. 7A than in Fig. 7B. Accordingly, the band in the FT in Fig. 7A is less intense than the IP band, suggesting that most of the TRIB2 antigen was caught by Ab/SC@MNPs and cleared from the FT. The strong band that resulted from the IP and the absence of a detectable band in the FT in Fig. 7B, suggests a complete capture of TRIB2-GFP protein by Ab/PDA@MNPs. This efficiency increment was caused by the elevated concentration of antibodies and the reduction of TRIB2 concentration in the prepared lysate. The last evaluated fraction was the WE; three primary antibodies were employed against GFP, ACTIN and GAPDH, which interacted with their specific proteins in the cellular extract.

The antibody against GFP detected the TRIB2-GFP fusion protein in the extract. On the other hand, the expression analysis of ACTIN and GAPDH confirmed that both protein extracts were loaded in the same amount in each lane and that the binding affinity of the homemade antibodies attached on the MNPs was significant, since they were able to differentiate and selectively react with TRIB2. Therefore, it was demonstrated that the anchored antibody on the coated MNPs was able to bind the target protein TRIB2 with high selectivity and efficiency.

4. Conclusions

Reproducible ultrafast and green syntheses of MNPs are reported within the present work, which were performed through the combination of high energy ultrasound and design of experiments (DOE). On the one hand, the high energy ultrasound reduces the environmental impact through the minimization of the employed energy, solvents and reagents. On the other hand, DOE allows making the sonochemical synthesis even more efficient in terms of applied energy (amplitude) and time of the synthesis. In fact, to the best of our knowledge, it is the first time in which MNPs are synthesized within one single minute with good reproducibility, higher saturation magnetization values (56–66 emu/g) and lower energy requirements (amplitude: 40% (2826 J)). The proper functionalization of MNPs was performed using organic species of different nature, including polymeric. Furthermore, several characterization techniques such as XRD, FTIR, TGA, SEM, TEM and VSM, were employed i) to characterize the composition, structure, size, morphology and magnetization of synthetized magnetic nanoparticles. This characterization confirmed the attainment of desirable magnetite nanoparticles mean size of 11 $\pm$ 2 nm with very uniform distribution; and ii) to reveal their applicability in the environmental field and biomedical sciences. Regarding the biosensing application, a linear relationship between the inhibitor concentration and the loss of catalytic activity of HRP was found (0.030 to 0.060 ppm Hg^{2+}; LOD/LOQ = 0.004/0.013 ppm), obtaining promising results aligned with the Environmental Protection Agency (0.002 ppm). The immunoprecipitation assays revealed the great potential of MNPs as a powerful and flexible tool for the characterization of protein function. In the present study, MNPs were customized to perform specific immunoprecipitations using a specific antibody against TRIB2. The IP results showed that using these tools a TRIB2-GFP fusion protein could be efficiently captured and precipitated from a complex cellular extract. Two approaches (Ab/SC, PDA@MNPs) proved to be suitable showing high specificity and efficacy. Additionally, efficiency was assessed with three primary antibodies (GFP, ACTIN and GAPDH) obtaining selective and specific answers of Ab/SC,PDA@MNPs. The customized MNPs described in this study will be employed to further characterize TRIB2 functions.

CRediT authorship contribution statement

Christian Hazael Pérez-Beltrán: Investigation, Methodology, Formal Analysis, Writing - Original Draft, Validation. **Juan José García-Guzmán:** Investigation, Formal Analysis, Writing- Reviewing and Editing. **Bibiana Ferreira:** Conceptualization, Visualization, Supervision, Writing- Reviewing and Editing. **Osvaldo Estévez-Hernández:** Methodology, Conceptualization, Visualization, Supervision. **David López-Iglesias:** Investigation, Formal Analysis, Writing- Reviewing and Editing. **Laura Cubillana-Aguilera:** Funding Acquisition, Resources, Writing- Reviewing and Editing. **Wolfgang Link:** Conceptualization, Visualization, Supervision, Writing- Reviewing and Editing. **N. Stănică:** Investigation, Formal Analysis, Writing- Reviewing and Editing. **Ana María dos Santos Rosa da Costa:** Conceptualization, Supervision, Funding Acquisition, Project Administration, Writing- Reviewing and Editing. **José María Palacios-Santander:** Conceptualization, Supervision, Funding Acquisition, Project Administration, Writing- Reviewing and Editing.

Declaration of competing interest

The authors declare that they have no known competing financial interests or personal relationships that could have appeared to influence the work reported in this paper.

Acknowledgments

Christian Hazael Pérez-Beltrán acknowledges Universidad Autónoma de Sinaloa (México) for funding and supporting with a scholarship his studies of the Erasmus Mundus Master in Quality in Analytical Laboratories (EMQAL) and the EMQAL consortium for the opportunity of performing this work. The Spanish authors greatly acknowledge Junta de Andalucía and Institute of Research on Electron Microscopy and Materials (IMEYMAT – BIOSENSEP and APPLIED-SENS projects) for their financial support and 'Programa de fomento e impulso de la investigación y de la transferencia de la Universidad de Cádiz 2018-2019' for the funds given through the projects PR2018-070 (Proyectos de Investigación-Puente 2018) and PR2020-013/SMAGAC (Proyectos de Investigación-Puente 2020). Dr. Osvaldo L. Estévez-Hernández thanks 'Programa de Movilidad Postdoctoral' funded by Asociación Universitaria Iberoamericana de Posgrado (AUIP) for his postdoc fellowship. This work was also supported by Fundação para a Ciência e a Tecnologia (FCT) Research Center Grant UID/BIM/04773/2013 Centre for Biomedical Research (CBMR), and UID/QUI/04023/2019 Algarve Chemistry Research Centre (CIQA), as well as by the Spanish Ministry of Science, Innovation and Universities through Grant RTI2018-094629-B-I00 to WL. BIF was supported by FCT-SFRH/BPD/100434/2014 and Marie Curie Individual Fellowship project TRIBBLES (#748585). This work was also supported by two LPCC-NRS/Terry Fox grants (2016/2017; 2017/2018).

Appendix A. Supplementary material

Supplementary material to this article can be found online at https://doi.org/10.1016/j.msec.2021.112023.

References

[1] R. Massart, Preparation of aqueous magnetic liquids in alkaline and acidic media, IEEE Trans. Magn. 17 (1981) 1247–1248.
[2] L. Shen, Y. Qiao, Y. Guo, S. Meng, G. Yang, M. Wu, J. Zhao, Facile co-precipitation synthesis of shape-controlled magnetite nanoparticles, Ceram. Int. 40 (2014) 1519–1524.
[3] H. Nosrati, M. Salehiabar, M. Fridoni, M.A. Abdollahifar, H.K. Manjili, S. Davaran, H. Anafar, New insight about biocompatibility and biodegradability of iron oide magnetic nanoparticles: stereological and in vivo MRI monitoring, Nat. Sci. Rep. 9 (7173) (2019) 1–10, https://doi.org/10.1038/s41598-019-43650-4.
[4] K. Tao, H. Dou, K. Sun, Interfacial coprecipitation to prepare magnetite nanoparticles: concentration and temperature dependence, Colloids Surfaces A Physicochem, Eng. Asp. 320 (2008) 115–122.
[5] M. Chen, Y. Cheng, The synthesis and surface modification of sc-MNPs for magnetic resonance imaging of stem cells, Nanomedicine Nanotechnology, Biol. Med. 14 (2018) 1855–1856.
[6] L. El Harrad, I. Bourais, H. Mohammadi, A. Amine, Recent advances in electrochemical biosensors based on enzyme inhibition for clinical and pharmaceutical applications, Sensors (Switzerland). 18 (2018) 1–25.
[7] E. Attari, H. Nosrati, H. Danafar, H.K. Manjili, Methotrexate anticancer drug delivery to breast cancer cell lines by iron oxide magnetic based nanocarrier, J Biomed Maater Res. 107 (2019) 2492–2500.
[8] S. Ahmed, B.L. Rajak, M. Gogoi, H.D. Sarma, Magnetic nanoparticles mediated cancer hyperthermia, in: Smart Healthc. Dis. Diagnosis Prev, Elsevier, 2020, pp. 153–173.
[9] N. Atar, T. Eren, M.L. Yola, H. Karimi-Maleh, B. Demirdögen, Magnetic iron oxide and iron oxide@gold nanoparticle anchored nitrogen and sulfur-functionalized reduced graphene oxide electrocatalyst for methanol oxidation, RSC Adv. 5 (2015), 26402.
[10] H. Alijani, M.H. Beyki, Z. Shariatinia, M. Bayat, F. Shemirani, A new approach for one step synthesis of magnetic carbon nanotubes/diatomite earth composite by chemical vapor deposition method: application for removal of lead ions, Chem. Eng. J. 253 (2014) 456–463.
[11] H.E. Rizk, N.E. El-Hefny, Synthesis and characterization of magnetite nanoparticles from polyol medium for sorption and selective separation of Pd(II) from aqueous solution, J. Alloys Compd. 812 (2020), 152041.

[12] A.E. Regazzoni, G.A. Urrutia, M.A. Blesa, A.J.G. Maroto, Some observations on the composition and morphology of synthetic magnetites obtained by different routes, J. Inorg. Nucl. Chem. 43 (1981) 1489–1493.

[13] A.A. Lahcen, A.A. Baleg, P. Baker, E. Iwuoha, A. Amine, Synthesis and electrochemical characterization of nanostructured magnetic molecularly imprinted polymers for 17-β-estradiol determination, Sens, Actuators B Chem. 241 (2017) 698–705.

[14] M.K. Poddar, M. Arjmand, U. Sundararaj, V.S. Moholkar, Ultrasound-assisted synthesis and characterization of magnetite nanoparticles and poly(methyl methacrylate)/magnetite nanocomposites, Ultrason, Sonochem. 43 (2018) 38–51.

[15] M. Ristić, E. Kuzmann, Z. Homonnay, S. Musić, Synthesis and properties of 1D manganese-doped hematite particles, J. Alloys Compd. 767 (2018) 504–511, https://doi.org/10.1016/j.jallcom.2018.07.115.

[16] R.M. Cornell, U. Schwertmann, The Iron Oxides: : Structure, Properties, Reactions, Occurrences and Uses, Second, Wiley-VCH, 2003.

[17] A.P.A. Faiyas, E.M. Vinod, J. Joseph, R. Ganesan, R.K. Pandey, Dependence of pH and surfactant effect in the synthesis of magnetite (Fe3O4) nanoparticles and its properties, J. Magn. Magn. Mater. 322 (2010) 400–404.

[18] A. Gałuszka, Z. Migaszewski, J. Namieśnik, The 12 principles of green analytical chemistry and the significance mnemonic of green analytical practices, TrAC Trends Anal. Chem. 50 (2013) 78–84.

[19] C. Bartolucci, A. Antonacci, F. Arduini, D. Moscone, L. Fraceto, E. Campos, R. Attaallah, A. Amine, C. Zanardi, L.M. Cubillana-Aguilera, J.M. Palacios-Santander, V. Scognamiglio, Green nanomaterials fostering agrifood sustainability, Trends Anal, Chem. 125 (2020), 115850.

[20] S.J. Doktycz, K.S. Suslick, Interparticle collisions driven by ultrasound, Science. 247 (1990) 1439–1445.

[21] M. Koel, Do we need green analytical chemistry? Green Chem. 18 (2016) 923–931.

[22] J.H. Bang, K.S. Suslick, Applications of ultrasound to the synthesis of nanostructured materials, Adv, Mater. (2010) 1039–1059.

[23] J.-X. Li, Z.-B. Qin, Y.-H. Li, G.-H. Cui, Sonochemical synthesis and properties of two new nanostructured silver(I) coordination polymers, Ultrason, Sonochem. 48 (2018) 127–135.

[24] R. Zarzuela, M.J. Luna, M.L.A. Gil, M.J. Ortega, J.M. Palacios-Santander, I. Naranjo-Rodríguez, J.J. Delgado, L.M. Cubillana-Aguilera, Analytical determination of the reducing and stabilization agents present in different Zostera noltii extracts used for the biosynthesis of gold nanoparticles, J. Photochem. Photobiol. B Biol. 179 (2018) 32–38.

[25] M.L.A. Gil, J.M. Palacios-Santander, J.J. Delgado, L.M. Cubillana-Aguilera, M. Franco-Romano, Sonosynthesis of gold nanoparticles from a geranium leaf extract, Ultrason, Sonochem. 21 (2014) 1570–1577.

[26] R.J. González-Álvarez, I. Naranjo-Rodríguez, M.P. Hernández-Artiga, J. M. Palacios-Santander, L. Cubillana-Aguilera, D. Bellido-Milla, Experimental design applied to optimisation of silica nanoparticles size obtained by sonosynthesis, J. Sol-Gel Sci. Technol. 80 (2016) 378–388.

[27] D. López-Iglesias, J.J. García-Guzmán, D. Bellido-Milla, I. Naranjo-Rodríguez, J. M. Palacios-Santander, L. Cubillana-Aguilera, The Sonogel-carbon-PEDOT material: an innovative bulk material for sensor devices, J. Electrochem. Soc. 165 (2018) B906–B915.

[28] A. Zamora-Gálvez, A. Ait-Lahcen, L.A. Mercante, E. Morales-Narváez, A. Amine, A. Merkoçi, Molecularly imprinted polymer-decorated magnetite nanoparticles for selective sulfonamide detection, Anal. Chem. 88 (2016) 3578–3584.

[29] V. Harnchana, A. Phuwongkrai, C. Thomas, V. Amornkitbamrung, Facile and economical synthesis of superparamagnetic magnetite nanoparticles coated with oleic acid using sonochemical route, Mater. Today Proc. 5 (2018) 13995–14001.

[30] T.M. Freire, L.M.U. Dutra, D.C. Queiroz, N.M.P.S. Ricardo, K. Barreto, J. C. Denardin, F.R. Wurm, C.P. Sousa, A.N. Correia, P. De Lima-Neto, P.B.A. Fechine, Fast ultrasound assisted synthesis of chitosan-based magnetite nanocomposites as a modified electrode sensor, Carbohydr, Polym. 151 (2016) 760–769.

[31] M. Carabajal, C.M. Teglia, S. Cerutti, M.J. Culzoni, H.C. Goicoechea, Applications of liquid-phase microextraction procedures to complex samples assisted by response surface methodology for optimization, Microchem. J. 152 (2020), 104436.

[32] I.M. Yusri, A.P.P. Abdul Majeed, R. Mamat, M.F. Ghazali, O.I. Awad, W.H. Azmi, A review on the application of response surface method and artificial neural network in engine performance and exhaust emissions characteristics in alternative fuel, Renew, Sustain. Energy Rev. 90 (2018) 665–686.

[33] C. Vasti, V. Pfaffen, E. Ambroggio, M.R. Galiano, R. Rojas, C.E. Giacomelli, A systematic approach to the synthesis of LDH nanoparticles by response surface methodology, Appl, Clay Sci. 137 (2017) 151–159.

[34] X. Liu, W. Liu, C. Wang, Z. Zheng, Optimization and modeling for one-step synthesis process of Ag–Cu nano-particles using DOE methodology, J. Mater. Sci. Mater. Electron. 27 (2016) 4265–4274.

[35] W.S. Peternele, V. Monge Fuentes, M.L. Fascineli, J. Rodrigues da Silva, R.C. Silva, C.M. Lucci, R. Bentes de Azevedo, Experimental investigation of the coprecipitation method: an approach to obtain magnetite and maghemite nanoparticles with improved properties, J. Nanomater. 2014 (2014) 1–10, https://doi.org/10.1155/2014/682985.

[36] V. Figueroa-Espí, A. Alvarez-Paneque, M. Torrens, A.J. Otero-González, E. Reguera, Conjugation of manganese ferrite nanoparticles to an anti Sticholysin monoclonal antibody and conjugate applications, Colloids Surfaces A Physicochem, Eng. Asp. 387 (2011) 118–124.

[37] C.H. Pérez-Beltrán, J.M. Palacios-Santander, A.M. dos Santos Rosa da Costa, Magnetic nanoparticles for biosensing and immunoprecipitation, Master Dissertation, Universidad de Cádiz, España; Universidade do Algarve, Portugal 2019.

[38] N.B. Messaoud, A.A. Lahcen, C. Dridi, A. Amine, Ultrasound assisted magnetic imprinted polymercombined sensor based on carbon black and gold nanoparticles for selective and sensitive electrochemical detection of Bisphenol A, Sensors and Actuators B, Chemical 276 (2018) 304–312, https://doi.org/10.1016/j.snb.2018.08.092.

[39] A.A. Lahcen, A.A. Baleg, P. Baker, E. Iwuoha, A. Amine, Synthesis and electrochemical characterization of nanostructured magnetic molecularly imprinted polymers for 17-β-estradiol determination, Sensors and Actuators B, Chemical 241 (2017) 698–705.

[40] P. Tartaj, C.J. Serna, Microstructural evolution of iron-oxide-doped alumina nanoparticles synthesized from microemulsions, Chem. Mater. 14 (2002) 4396.

[41] B.L. Cushing, V.L. Kolesnichenko, C.J. O'Connor, Recent advances in the liquid-phase syntheses of inorganic nanoparticles, Chem. Rev. 104 (2004) 3893, https://doi.org/10.1021/cr030027b.

[42] E. Morgan, Chemometrics: Experimental design, J. Chemom. 10 (1996) 349.

[43] D.C. Montgomery, Diseño y análisis de experimentos, Limusa Wiley, 2003.

[44] I. Martínez-Mera, M.E. Espinosa-Pesqueira, R. Pérez-Hernández, J. Arenas-Alatorre, Synthesis of magnetite (Fe3O4) nanoparticles without surfactants at room temperature, Mater. Lett. 61 (2007) 4447–4451.

[45] S. El-Guendouz, S. Aazza, B. Lyoussi, V. Bankova, J.P. Lourenço, A.M. Rosa Costa, J.F. Mariano, M.G. Miguel, M.L. Faleiro, Impact of biohybrid magnetite nanoparticles and moroccan propolis on adherence of methicillin resistant strains of staphylococcus aureus, Molecules. 21 (2016) 1–18.

[46] M.I. Khalil, Co-precipitation in aqueous solution synthesis of magnetite nanoparticles using iron(III) salts as precursors, Arab, J. Chem. 8 (2015) 279–284.

[47] D.R. Dreyer, D.J. Miller, B.D. Freeman, D.R. Paul, C.W. Bielawski, Elucidating the structure of poly(dopamine), Langmuir. 28 (2012) 6428–6435.

[48] M. Tarantash, H. Nosrati, H.K. Manjili, A.B. Khoshfetrat, Preparation, characterization and *in vitro* anticancer activity of paclitaxel conjugated magnetic nanoparticles, Drug Dev, Ind. Pharm. 44 (11) (2018) 1895–1903.

[49] K. Petcharoen, A. Sirivat, Synthesis and characterization of magnetite nanoparticles via the chemical co-precipitation method, Mater, Sci. Eng. B Solid-State Mater. Adv. Technol. 177 (2012) 421–427.

[50] S. Chang, K.-Y.A. Lin, C. Lu, Efficient adsorptive removal of Tetramethylammonium hydroxide (TMAH) from water using graphene oxide, Sep, Purif. Technol. 133 (2014) 99–107.

[51] Y. Lee, M.-H. Ryou, M. Seo, J.W. Choi, Y.M. Lee, Effect of polydopamine surface coating on polyethylene separators as a function of their porosity for high-power Li-ion batteries, Electrochim. Acta 113 (2013) 433–438.

[52] H. Sharifi Dehsari, V. Ksenofontov, A. Möller, G. Jakob, K. Asadi, Determining magnetite/maghemite composition and core-shell nanostructure from magnetization curve for iron oxide nanoparticles, J. Phys. Chem. C. 122 (2018) 28292–28301.

[53] G. Bukhtiyarova, M. Kazakova, O.A. Bayukov, Facile synthesis of nanosized ε-Fe2O3 particles on the silica support, Artic, J. Nanopart. Res. 13 (2011) 5527–5534.

[54] H. Yan, K. Liu, S. Wan, J. Huang, Size-controlled preparation of magnetite nanoparticles in the presence of graft copolymers, J. Mater. Chem. 16 (2006) 298–303.

[55] M. Martín, P. Salazar, R. Villalonga, S. Campuzano, J.M. Pingarrón, J.L. González-Mora, Preparation of core-shell Fe3O4@poly(dopamine) magnetic nanoparticles for biosensor construction, J. Mater. Chem. B 2 (2014) 739–746.

[56] W. Link, Tribbles breaking bad: TRIB2 suppresses FOXO and acts as an oncogenic protein in melanoma, Biochem. Soc. Trans. 43 (2015) 1085–1088, https://doi.org/10.1042/BST20150102.

[57] F. Zanella, O. Renner, B. García, S. Callejas, A. Dopazo, S. Peregrina, A. Carnero, W. Link, Human TRIB2 is a repressor of FOXO that contributes to the malignant phenotype of melanoma cells, Oncogene 29 (2010) 2973–2982, https://doi.org/10.1038/onc.2010.58.

[58] R. Hill, P.A. Madureira, B. Ferreira, I. Baptista, S. Machado, L. Colaço, M. dos Santos, N. Liu, A. Dopazo, S. Ugurel, A. Adrienn, E. Kiss-Toth, M. Isbilen, A. O. Gure, W. Link, TRIB2 confers resistance to anti-cancer therapy by activating the serine/threonine protein kinase AKT, Nature Comm. 8 (2017) 14687, https://doi.org/10.1038/ncomms14687.

[59] R. Hill, R. Kalathur, S. Callejas, L. Colaço, R. Brandão, B. Garcia Serelde, A. Cebriá, C. Blanco-Aparicio, J. Pastor, M. Futschik, A. Dopazo, W. Link, A novel phosphatidylinositol 3-kinase (PI3K) inhibitor directs a potent FOXO-dependent, p53-independent cell cycle arrest phenotype characterized by the differential induction of a subset of FOXO-regulated genes, Breast Cancer Res. 16 (2014) 482, https://doi.org/10.1186/s13058-014-0482-y.